Journal of Materials Chemistry C
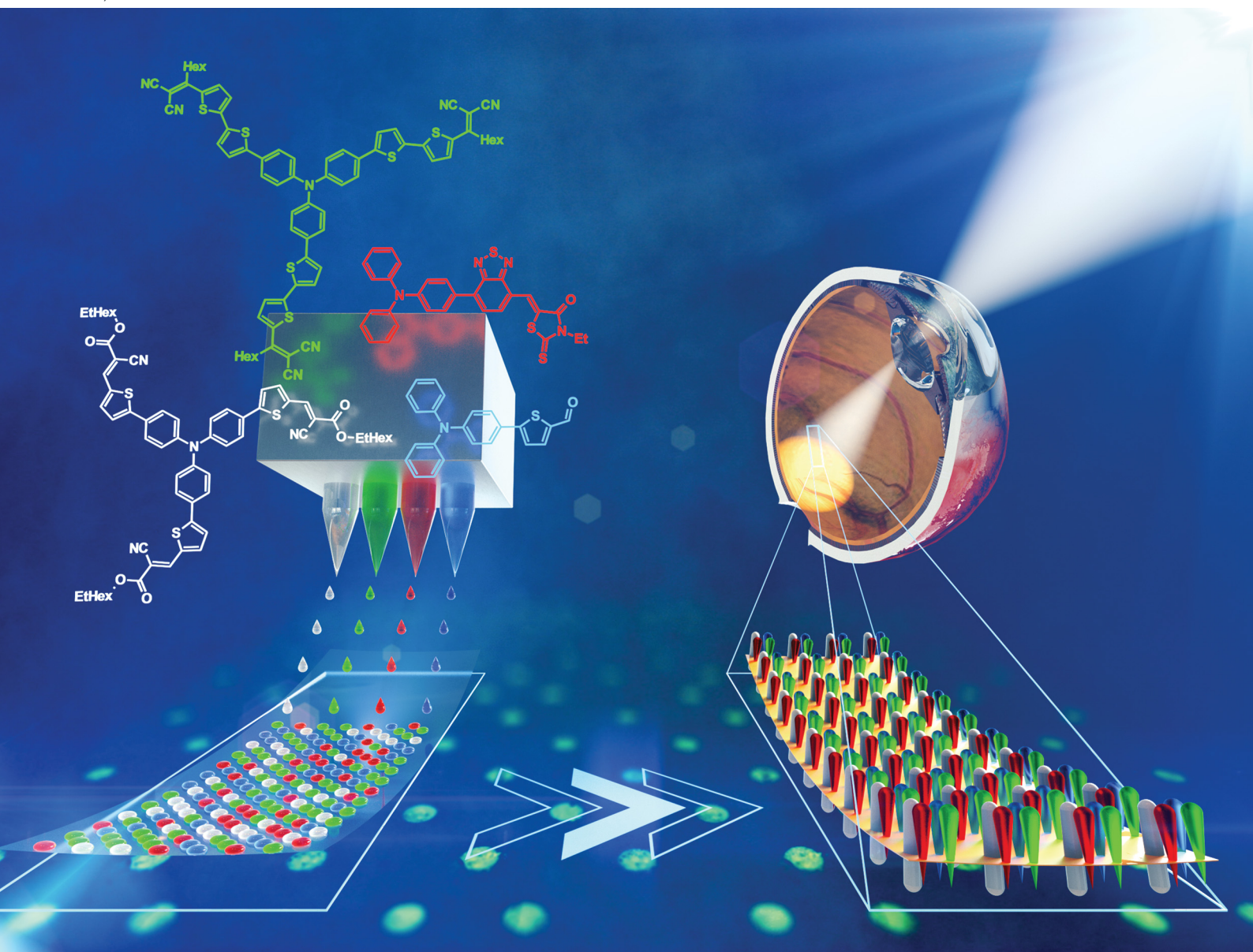
Materials for optical, magnetic and electronic devices

rsc.li/materials-c

ROYAL SOCIETY
OF CHEMISTRY

COMMUNICATION
M. Skhunov, S. A. Ponomarenko *et al.*
Pixelated full-colour small molecule semiconductor devices
towards artificial retinas

COMMUNICATION

Check for updates

Pixelated full-colour small molecule semiconductor devices towards artificial retinas†

M. Skhunov, [ID] *[a] A. N. Solodukhin,[b] P. Giannakou, [ID] [a] L. Askew,[a]
Yu. N. Luponosov, [ID] [b] D. O. Balakirev,[b] N. K. Kalinichenko,[b] I. P. Marko,[c]
S. J. Sweeney[c] and S. A. Ponomarenko [ID] *[b]

Opto-stimulation of semiconductor-biointerfaces provides efficient pathways towards eliciting neural activity through selective spectral excitation. In visual prosthesis, tri-colour stimulation capability is the key to restoring full-colour vision. Here we report on investigation of organic photoactive π-conjugated donor–acceptor small molecules based on triphenylamine whose absorption spectra are similar to those of the photoreceptors of the human eye. Photoactive device fabrication and characterisation towards full colour, pixelated retinal prosthesis based on inkjet printing of these molecules is demonstrated, with round pixels reaching 25 microns in diameter. Photo-response is studied *via* interfacing with biological electrolyte solution and using long-pulse, narrow-band excitation. Both photo-voltage and photo-current responses in the devices with a ZnO hole-blocking interlayer show clear signatures of capacitive charging at the electrolyte/device interface, also demonstrating spectral selectivity comparable to that of human eye' cones and rods.

1. Introduction

Visual impairment according to the World Health Organization affects at least 1 billion people worldwide living with conditions ranging from mild disability to blindness.[1,2] One of the leading global causes of visual deficiency is age-related macular degeneration (AMD), caused by damage to the macula of the retina due to the gradual degradation of cone cells.[3] Another disease mostly affecting rod cells is retinitis pigmentosa (RP) that is passed through faulty genes.[4,5] In both cases of AMD and RP, photoreceptor cells are mostly affected, whereas the neural tissue

remains mainly functional, thus opening opportunities for retinal prosthetic devices. Significant research efforts have been devoted to developing retinal implants in both epi-retinal and sub-retinal configurations to restore some level of vision in those with conditions causing severe retinal degeneration. In epi-retinal implants,[6] the image is captured and digitised by an external video device and electrical signals are transferred to an array of micro electrodes attached to the remaining functioning inner neurons of the retina. Issues encountered in this approach include the requirement for a power supply to the electronics in the eye and wiring to connect the external image-capturing device, which entails complex surgical procedures as well as a significant level of discomfort during use. The alternative subretinal approach[7] involves implanting an array of photovoltaic pixels between the bipolar cell layer and the retinal pigment epithelium. The implanted photovoltaics directly replace the damaged photoreceptors with the assumption that the other neural cells continue to function normally. The advantage of this approach is that no wiring and external power supply to the eye is required and the implanted devices are entirely self-powered. The main complication associated with inorganic-based retinal implant devices is biocompatibility.

Organic-based semiconductor devices that have been developed in the recent years are expected to be substantially more user-friendly due to the potentially excellent bio-compatibility of carbon-based molecules and human tissues.[6,7] Organic semiconductors are mechanically flexible,[8] chemically tunable, and solution-processable, and they have easily modifiable surface structure.[9–11] Smart surfaces with switchable adhesion can be chemically tuned to be biocompatible with anti-biofouling behavior.[12] Some of them possess a mixed ionic and electronic conductivity, which can reduce the impedance at the electronic-biological system interfaces and enhance electrical signal collection.[11,13,14]

Organic semiconductors, including π-conjugated polymers, have been successfully demonstrated in photovoltaic type device configuration[15] to elicit neural activity during photo-excitation. Importantly, these carbon based molecules have

[a] Electrical and Electronic Engineering, Advanced Technology Institute, University of Surrey, Guildford, UK. E-mail: m.shkunov@surrey.ac.uk

[b] Enikolopov Institute of Synthetic Polymeric Materials of the Russian Academy of Sciences, Profsoyuznaya st. 70, Moscow 117393, Russia. E-mail: ponomarenko@ispm.ru

[c] Advanced Technology Institute and Department of Physics University of Surrey, Guildford, GU2 7XH, UK

† Electronic supplementary information (ESI) available. See DOI: 10.1039/d0tc05383j

good affinity to biological systems,[16] and also demonstrate excellent photoresponse, some of the highest absorption coefficients in the 10^5 cm^{-1} range,[17,18] and electronic and ionic conductivity, and allow an intimate interface with a liquid bioenvironment.

K. S. Narayan's group[19] has demonstrated that it is possible to stimulate the blind retina of embryonic chicks that lack light sensitivity at this stage of development. When this retina was placed on a mixture of P3HT with a naphthalene acceptor deposited on a commercial multi-electrode array (MEA), light response signals were observed that are characteristic of the retina with developed photoreceptors. Maya-Vetencourt et al.[15] reported the development and validation of a fully organic prosthesis for long-term in vivo intra-retinal implantation into the eye of retinitis pigmentosa rats. The implant consisted of silk threads on which layers of semiconducting polymers PEDOT:PSS and P3HT were applied. Electrophysiological and behavioural analysis revealed restoration of light sensitivity and visual acuity caused by the prosthesis. These effects persisted up to 6–10 months after surgery. In a recent work, the same group showed that P3HT nanoparticles (NPs P3HT) promote light-dependent activation of retinal neurons and restore visual function upon subretinal injection in a rat model of retinitis pigmentosa.[20]

Despite significant progress with π-conjugated polymer retinal prosthesis, only 'monochrome' vision capability has been demonstrated. Some suggestions have been made regarding the possibility of multi-colour colorimetric sensors, including demonstration of tri-colour, all solid state conjugated polymer photodiodes operating in air,[21] and bulk-heterojunction, single layer polymer devices with transient output signal polarity and temporal signal profiles being specific to various excitation wavelengths.[22]

Overall, the task of restoring full colour vision remains highly relevant. For a subretinal implant to enable colour vision restoration, it is expected that (i) the distribution of red, green, and blue 'cone' and 'rod' photopixels will approximately resemble that of a typical human retina, and (ii) in the case of AMD or RP, some degree of alignment between the remaining live neural cells, being previously 'connected' to a particular colour type of cones and rods, and the prosthetic device colour pixels of the exact colour is achievable after the implantation. It is challenging to achieve both outcomes; however, device fabrication techniques such as inkjet printing allow one to produce customisable, high resolution patterns of functional materials that can foreseeably mimic even individual patient's distribution of various cone cells. Positioning of prosthetic individual colour pixels to overlap with the corresponding colour neural tissue cell is certainly more challenging. Neural plasticity or the ability of the brain to adapt and to compensate for the changes in sensory inputs is considered to be the key for the rehabilitation following artificial retina implantation,[23] which can potentially allow patients to re-learn and to re-gain tri-colour vision capability, should they be offered by the prosthetic device.

In this study we have focused on organic small π-conjugated molecules with various optical bandgaps aiming to reproduce

absorption characteristics of human retina rod and cone cells. As compared to semiconductor polymer materials, small molecules have a number of advantages including ease of purification, well-defined molecular structure, complete lack of polydispersity, so common to polymers, and a very high degree of repeatability in relation to chemical synthesis, allowing nearly identical reproducibility of all their characteristics from batch to batch.[18,24]

Among organic semiconductor materials, donor–acceptor molecules have the most promising properties due to excellent light absorption, high stability and good solubility in organic solvents. Varying the donor and acceptor functionalities allows fine-tuning of their absorption bands.[25,26] Triphenylamine is one of the most popular electron donor blocks, allowing the production of small molecules of various architectures from linear to star-shaped.[18,27,28] Many triphenylamine derivatives show good biocompatibility.[29–32] Recently single-component organic photodetectors with a relatively narrow responsivity spectrum based on π-conjugated donor–acceptor (D–A) molecules with a triphenylamine electron donor core have been described.[33] Similar molecules with absorption spectra being close to the photosensitivity response of photoreceptors (blue cones, rods, green cones, red cones) can be used for creating full colour retinal prosthesis devices.

To provoke a neural response in retinal prosthetics, literature results indicated various levels of charge transfer to take place in the range of 0.1 to 1 mC cm^{-2} within 1–20 ms.[34] The device must also overcome biocompatibility issues including the potential effect of the electronics (such as heating) on the retina.[35,36] The number of pixels required for vision restoration to a level where the individual could read with visual aid (20/100 vision) has been estimated to be at least 600 with a pixel size below 25 μm. A pixel size of around 5 μm is required for 20/20 vision with the pixels arranged on a small disk, a few millimetres in diameter.[37]

In this work we present a feasibility study towards full-colour artificial retina devices to replace tri-colour cones, and also rods, in the form of future subretinal prosthetic devices on flexible substrates. The choice of photoactive materials was motivated by the photoresponse characteristics of human blue ('S' – short), green ('M' – medium) and red ('L' – long) cones and also rod cells (Fig. 1a and b). The potential of pixelated devices is demonstrated by inkjet printed small molecule arrays, with pixel diameters reaching 25–30 microns. An attempt is made to spectrally reproduce the photo-induced response of cones and rods in the form of photo-current and photo-voltage spectra obtained from devices, each containing one of the four organic conjugated molecules, interfaced with an electrolyte (phosphate buffered saline, PBS), thus aiming to simulate a biological environment (Fig. 1c and d). Further device optimisation is achieved by interfacial engineering and reducing the barrier to electron collection at the indium tin oxide (ITO) electrode surface via applying the ZnO interlayer leading to a more than 20 times increase in photocurrent as compared to bare ITO surface devices. Importantly, ZnO contributes to mostly capacitive response of the devices to photoexcitation.
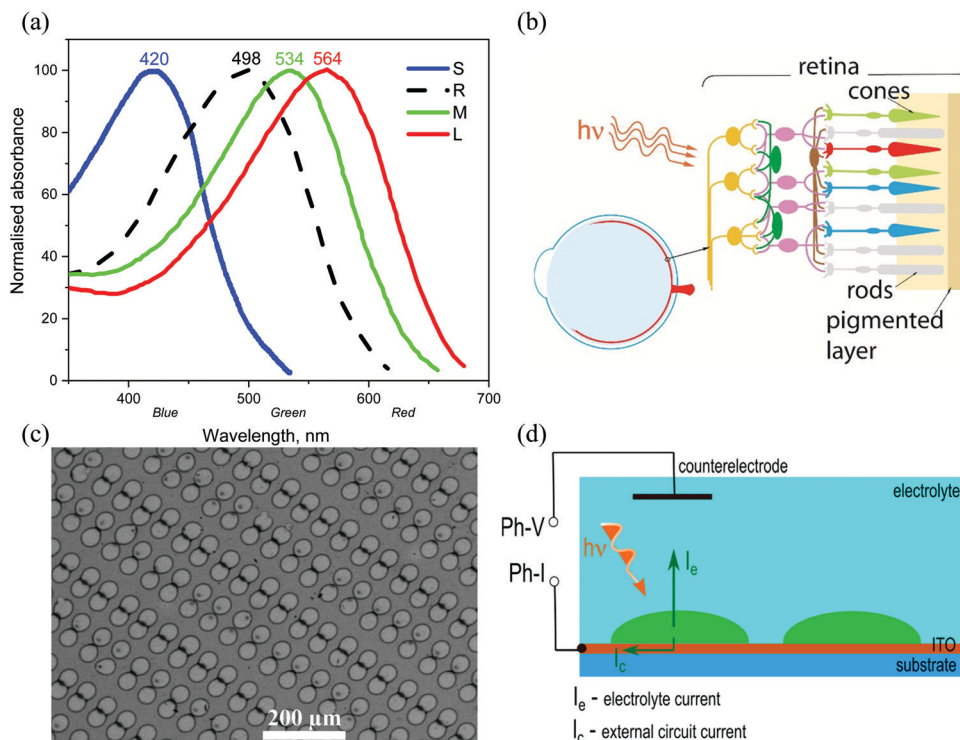
This journal is © The Royal Society of Chemistry 2021

J. Mater. Chem. C, 2021, 9, 5858–5867 | 5859

Fig. 1 (a) Spectral absorption curves of the short (S), medium (M) and long (L) wavelength pigments in human cones, corresponding to blue, green and red absorption bands respectively, and rod (R) cells,[38–40] (b) schematic of an eye, and retina cross-section showing neurons connected to rods and cones, (c) scanning electron microscope (SEM) image of inkjet printed, red absorbing organic pixels in this work, at 375× magnification, (d) photo-induced current flow diagram for pixelated conjugated molecule devices interfaced with an electrolyte (PBS). Both photo-voltage (Ph-V) and photo-current (Ph-I) can be recorded with this schematic.

2. Results and discussion

2.1. Choice of materials for simulating absorption of human cones and rods

Among the available extensive library of donor–acceptor compounds based on triphenylamine, molecules that met the following criteria were selected: molecules whose thin films showed absorption spectra that matched the photosensitivity of human photoreceptors, as well as sufficient solubility for the preparation of inkjet inks. Fig. 2 shows the chemical structures of π-conjugated donor–acceptor molecules investigated in this work. The synthesis and characterization of **TPA-T-C(O)H** (blue), **N(Ph-2T-DCV-Hex)₃** (green), **N(Ph-T-CNA-EtHex)₃** (rods) and **TPA-BTZ-Rh-Et** (red) are described in the ESI.†
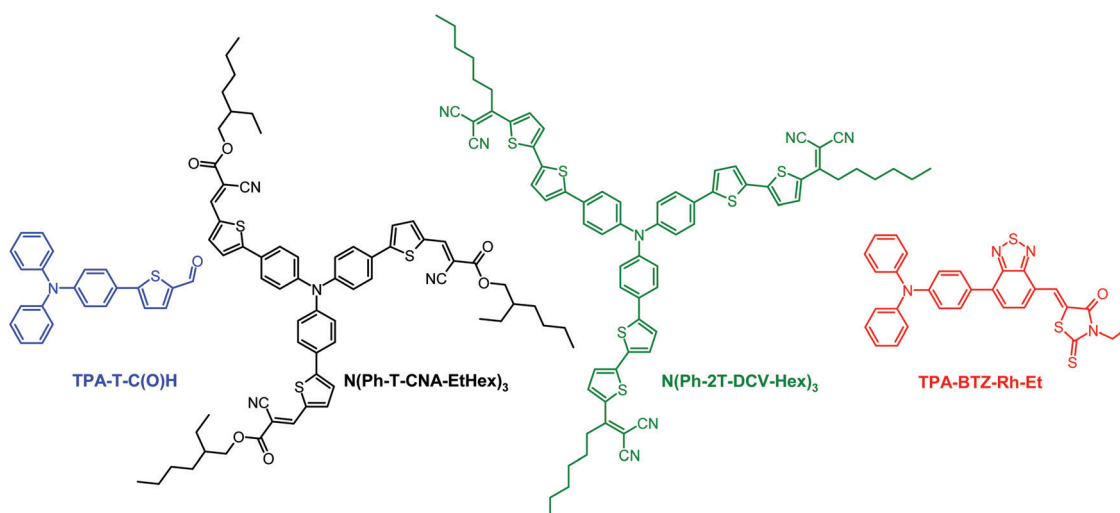

Fig. 2 Chemical structures of D−A molecules **TPA-T-C(O)H**, **N(Ph-T-CNA-EtHex)₃**, **N(Ph-2T-DCV-Hex)₃**, and **TPA-BTZ-Rh-Et**.

5860 | *J. Mater. Chem. C*, 2021, **9**, 5858–5867

This journal is © The Royal Society of Chemistry 2021

Fine-tuning of the absorption spectrum of the presented series of molecules is based on a combination of a triphenylamine block with electron-withdrawing groups of various strength with or without a thiophene π-spacer. The absorption spectra of the compounds in diluted THF solutions (Table 1 and Fig. S8 in the ESI†) have two types of absorption bands: the band in the short wavelength region (280–430 nm) is usually attributed to the π–π* transition in the conjugated phenylene-thiophene fragment and the intense absorption band in the long-wavelength region (370–600 nm) is usually attributed to intramolecular charge transfer (ICT) between the electron-donating triphenylamine and electron-withdrawing blocks.[41,42] Albeit recently it was shown that they have a mixed character.[43] A combination of a relatively weak electron-withdrawing aldehyde group through a monothiophene π-spacer with triphenylamine was used in the case of blue cones' analogues. According to density functional theory (DFT) calculations (Table 1 and Table S3 in the ESI†) and cyclic voltammetry (CV) measurements (Table 1), this molecular design resulted in the highest LUMO and bandgap values compared to the other materials. When the electron-withdrawing aldehyde group of **TPA-T-C(O)H** was replaced by a stronger cyanoacetate one and the structure was modified from linear to star-shaped, it led to **N(Ph-T-CNA-EtHex)₃** having a decreased LUMO value and the band gap as well as the red-shifted absorption spectrum similar to that of the rods (Table 1). A further decrease in the LUMO value was achieved by replacing cyanoacetate electron-withdrawing groups with the stronger dicyanovinyl ones.[44] Replacement of a monothiophene π-spacer with a bithiophene one led to an increase of the HOMO value and an even greater decrease of the band gap value, thus making the absorption spectrum of **N(Ph-2T-DCV-Hex)₃** similar to that of the green cones. To match the absorption spectrum of the red cones, the triphenylamine block was linked with a combination of two electron-withdrawing blocks based on 2,1,3-benzothiadiazole and N-ethylrhodanine. This led to the **TPA-BTZ-Rh-Et** molecule with the lowest LUMO value and the longest wavelength absorption maximum among the compounds under consideration (Table 1).

The compounds were chosen due to their absorption maxima positions being close to that of human cones and rods (420 nm, 534 nm, and 564 nm for blue, green and red cones respectively, and 498 nm for rods).[40] Normalised absorption spectra for the four compounds' thin films, spin-coated from THF solutions (5–10 mg mL⁻¹), are presented in Fig. 3 (for preparation and as-recorded data refer to the ESI†), showing good overlap with that of human photoreceptors (Fig. 1a). The absorption maxima of **TPA-T-C(O)H** and **N(Ph-2T-DCV-Hex)₃** overlap well with that of blue and green cones, whereas **TPA-BTZ-Rh-Et** absorbing in the red spectral region has somewhat shorter wavelength peak absorption at 548 nm as compared to the red cone peak (564 nm). Considering that the peak absorption value of cones for different people can vary by up to +/−10 nm,[38] exact overlap between the synthetic compound's absorption and that of the human cone cells and rods might not be necessary. A small blue-absorption peak at 400 nm of the compound **TPA-BTZ-Rh-Et** did not seem to be significant, as further photo-action experiments did not show noticeable photocurrent signals around this wavelength.

Although optical absorption data provide useful information, spectral photo-response of samples immersed in an electrolyte is essential for identifying materials for future retinal prosthesis, considering these tests being closer to a realistic biological environment.

2.2. Spectral photo-response for semiconductor/electrolyte devices

Organic small molecule samples were deposited on glass/ITO/ZnO substrates, and were mounted inside a cuvette filled with the electrolyte typically used to simulate biological environments – Phosphate-Buffered Saline (PBS). The electrical signal in the form of photocurrent or photovoltage was recorded using a lock-in amplifier using a phase-sensitive detection technique, while the sample was exposed to a monochromatic light source with low power output, not exceeding 200 microwatts at the peak absorption wavelength range of 400–570 nm (see ESI†). The wavelength was scanned from typically 300 nm to up to 900 nm in 1 nm or 2 nm steps, with a monochromated linewidth of 3 nm (full width at half maximum), and photo-induced signal spectra were recorded for all four materials. Spectral response data, corrected for the system response, were collected for thicker drop-cast deposited samples, thinner spin-coated samples, and a range of samples with inkjet printed layers, and also printed isolated pixels, aiming to approach the spectral response of human photoreceptors.

A schematic of the electrolyte filled cell is shown in Fig. 4a, where the ITO/ZnO contact served as a signal electrode and a

Table 1 Optical, electrochemical, DFT and photocurrent spectra data

| Compound | Optical data | | | | | | CV[e] | | | DFT[f] | | |
| | Solution[a] | | | Film[b] | | | | | | | | |
	λ_{max}, nm	λ_{onset}[c], nm	E_g^{opt}[d], eV	λ_{max}, nm	λ_{onset}[c], nm	E_g^{opt}[d], eV	HOMO, eV	LUMO, eV	E_g, eV	HOMO, eV	LUMO, eV	E_g, eV
BC	400	449	2.76	424	491	2.52	−5.42	−2.81	2.61	−5.05	−1.84	3.21
R	482	548	2.26	504	586	2.11	−5.43	−3.35	2.08	−5.34	−2.70	2.64
GC	501	591	2.09	533	659	1.88	−5.34	−3.41	1.93	−5.36	−3.03	2.33
RC	514	604	2.03	548	660	1.88	−5.40	−3.47	1.93	−5.09	−2.90	2.19

Notes: BC (TPA-T-C(O)H), R (N(Ph-T-CNA-EtHex)₃), GC (N(Ph-2T-DCV-Hex)₃), RC (TPA-BTZ-Rh-Et). [a] Measured in diluted THF solution. [b] Cast from THF solution. [c] Determined as an intersection between the tangent to the absorption edge and the abscissa axis. [d] Bandgap estimated from the onset wavelength (λ_{onset}) of the optical absorption: $E_g^{opt} = 1240/\lambda_{onset}$. [e] Measured in thin films. [f] Calculated by the DFT method.

This journal is © The Royal Society of Chemistry 2021

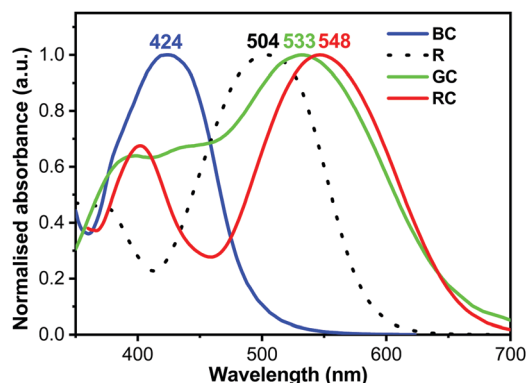J. Mater. Chem. C, 2021, **9**, 5858–5867 | **5861**

Fig. 3 Normalised absorption spectra of thin films on glass **TPA-T-C(O)H** (BC), **N(Ph-T-CNA-EtHex)₃** (R), **N(Ph-2T-DCV-Hex)₃** (GC), and **TPA-BTZ-Rh-Et** (RC).

gold needle was used as a counter (ground) electrode. The samples were exposed to the beam, through the electrolyte filled cell. Photo-induced signal *versus* wavelength spectra were recorded in either photovoltage (open circuit) mode or photo-current (short circuit) mode of a lock-in amplifier.

Typically, a heterojunction interface is required to split photo-excited electron–hole pairs, excitons, and in our case the properties of the substrate/small molecule interface demonstrated a strong influence on the intensity of photocurrent and photovoltage produced, pointing out that this interface is mostly responsible for charge separation in our devices with thin organic layers. All the results presented in this section were obtained for glass/ITO/ZnO substrates, giving rise to the highest photo-current/voltage responses. More detailed discussion of charge separation and the effect of substrate work function on the photosignal is presented in Section 2.5.

Photo-response spectra were obtained for four materials and typical photocurrent spectra are shown in Fig. 4b for the

samples spin-coated on glass/ITO/ZnO substrates. Overall, all photocurrent spectra of the thin films demonstrate a red-shift for peak response wavelengths as compared to absorption data of the same molecules. Nevertheless, the photoaction spectra bear a very good resemblance to the response characteristics of human cones and rods. Just one molecule, **N(Ph-T-CNA-EtHex)₃**, demonstrated a more than 20 nm shift of the peak wavelength *versus* rods' photoaction spectra. Further results on photo-voltage responses of the small molecules are presented in the ESI.† The magnitude of maximum photocurrent obtained from a set of typical samples is given in Table 2.

The blue absorbing material, **TPA-T-C(O)H**, demonstrated photocurrent in the range of 100 nA (for current sample setup geometry). Two materials with absorption in the blue-green and green part of the spectrum, **N(Ph-T-CNA-EtHex)₃** and **N(Ph-2T-DCV-Hex)₃**, showed a significantly higher level of photocurrent around 1 μA, resulting in an estimated current density of 14 μA cm^{-2}. The red absorbing material **TPA-BTZ-Rh-Et** had a lower level of response as compared to the other small molecules. Such behaviour of photo-sensitive materials would be reminiscent of that of human cones and rods, where a lower response level is typical for blue and red cones, and a much higher response level is observed for rods and green cones.

2.3. Inkjet printed pixelated devices

The key for colour-pixel device fabrication is inkjet printing, offering excellent opportunities for direct deposition of the conjugated molecules in desired patterns, at low temperature (30 °C), requiring no post-processing steps, where the smallest diameter of printed pixels is defined by the ejected droplet volume, viscosity of the ink and wettability of the substrate. Our studies demonstrated that 20–35 micron diameter pixels can be obtained with a typical materials printer, being comparable to artificial retina resolution requirements of 25 micron pixels for restoring 20/100 vision.[37] Smaller diameters can be obtained by
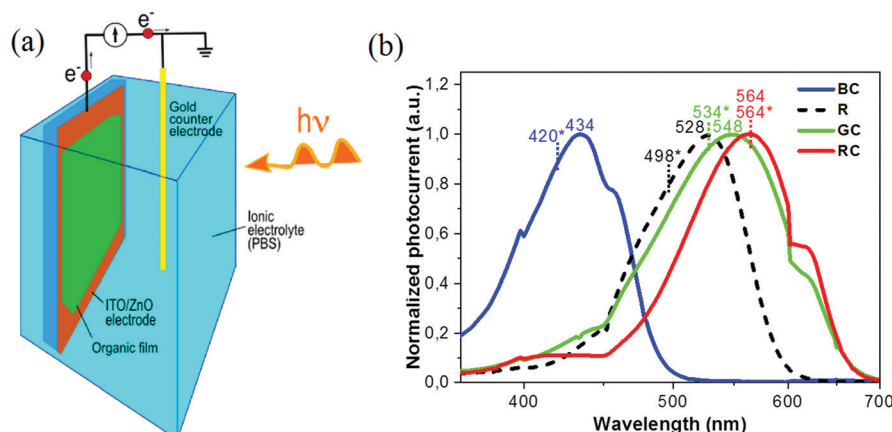

Fig. 4 (a) Schematic of the electrolyte filled cell for photocurrent and photovoltage measurements, (b) Typical normalised photocurrent spectra of thin films spin coated on glass/ITO/ZnO substrates, interfaced with an electrolyte (PBS). Spectra corresponding to three materials (**TPA-T-C(O)H** (BC), **N(Ph-2T-DCV-Hex)₃** (GC), **TPA-BTZ-Rh-Et** (RC)) expecting to simulate cones' sensitivity profiles are represented by bold lines. The dashed line curve corresponds to the **N(Ph-T-CNA-EtHex)₃** (R) sample aiming to resemble rods' response. The spectral response maxima of human photoreceptors are represented by dotted vertical lines marked with an asterisk * (420 nm, 498 nm, 534 nm, 564 nm). (The sharp spike at ∼400 nm and a 'dip' at 600 nm are due to changes in the spectrometer grating at these wavelengths.)

5862 | J. Mater. Chem. C, 2021, 9, 5858–5867

This journal is © The Royal Society of Chemistry 2021

Table 2 Photocurrent spectra maxima and current's maximum values obtained for thin films of materials (spin coated on glass/ITO/ZnO)

Compound	Absorption maximum (nm)	Photocurrent (nA)
TPA-T-C(O)H	434	101
N(Ph-T-CNA-EtHex)$_3$	528	1050
N(Ph-2T-DCV-Hex)$_3$	548	1246
TPA-BTZ-Rh-Et	564	30

using higher viscosity inks and the corresponding jetting equipment.[45]

Pixelated samples were produced with the small molecules dissolved in tetralin at 20 mg mL^{-1} concentration. Printing was performed with 1 pL and also 10 pL heads/cartridges on glass/ITO/ZnO substrates, and also the same types of substrates coated with an ultrathin (20 nm) layer of polystyrene. Printing parameters have been adjusted to allow single droplet jetting to deposit an array of isolated pixels. Overall, over 30 samples have been fabricated. Fig. 5(a and b) shows optical microscope images of a fragment of the **TPA-BTZ-Rh-Et** (red) small molecule array with 42 μm diameter pixels and the **N(Ph-T-CNA-EtHex)$_3$** ('rod') array with ~25 μm diameter pixels. Higher resolution

images have been obtained with SEM (Fig. 5c). Depending on the inkjet droplet size, viscosity of the ink and substrate surface conditions, printed pixels were produced with a range of diameters from 70 microns for 10 pL cartridges to ~20 microns for 1 pL cartridges. Pixelated samples were stable in the electrolyte environment and did not delaminate during the measurements. Photocurrent measurements (Fig. S10(b), ESI†) were conducted with the samples prepared from all four molecules, and typical data are presented in Fig. 5d. Photo-action spectra resembled, in general, that of the thin films, although peak positions were slightly shifted, at 432 nm (blue), 511 nm ('rods'), 530 nm (green) and 540 nm (red). We speculate that some variations in the position of photoresponse peaks might have resulted from small changes in the films' morphology and molecular packing due to differences in processing, including solvents (chlorobenzene vs tetralin), drying kinetics (spin-coating vs inkjet printing) and the way films and printed pixels dry on the substrates.

X-Ray diffraction data of thin films obtained from tetralin solution showed that all of them are amorphous, regardless of the shape of the molecules and the type of electron-withdrawing fragments. In all cases, only a diffuse halo was observed on the diffraction curves (Fig. S16, ESI†).
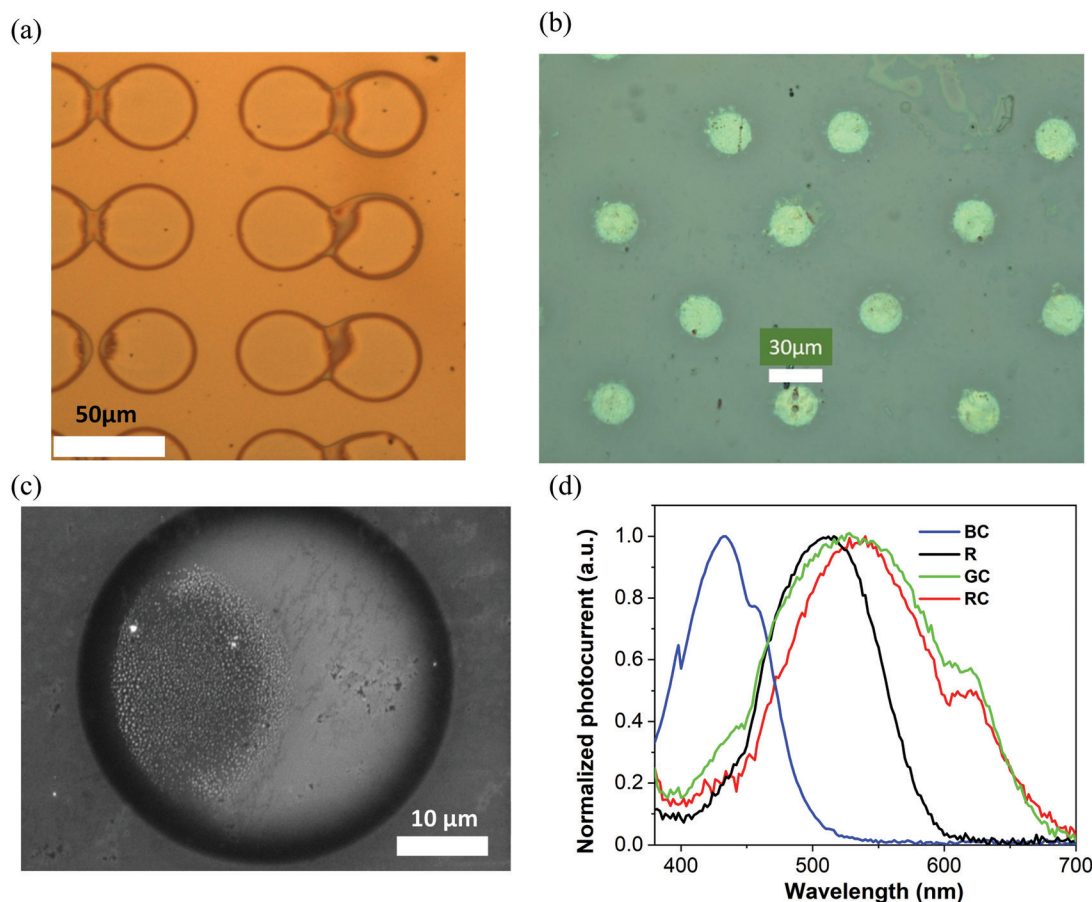

Fig. 5 Optical microscope image of the (a) **TPA-BTZ-Rh-Et** pixel array (~42 μm diameter) and (b) **N(Ph-T-CNA-EtHex)$_3$** array (~25 μm diameter), (c) SEM image of a **TPA-BTZ-Rh-Et** single pixel 42 μm in diameter, at 725 k magnification, and (d) typical normalised photocurrent spectra of inkjet printed small molecule pixels on glass/ITO/ZnO substrates, interfaced with an electrolyte (PBS). Peak position wavelengths are 432 nm (blue), 511 nm ('rods'), 530 nm (green) and 540 nm (red).

This journal is © The Royal Society of Chemistry 2021

J. Mater. Chem. C, 2021, **9**, 5858–5867 | **5863**

As compared to human photoreceptors' spectral response maxima (420 nm, 498 nm, 534 nm, 564 nm), printed pixel arrays demonstrated reasonable correlation, that only differed by ∼12–13 nm for **TPA-T-C(O)H** (blue) and **N(Ph-T-CNA-EtHex)₃** ('rods'), and within 4 nm for **N(Ph-2T-DCV-Hex)₃** (green). **TPA-BTZ-Rh-Et** (red) molecules showed a larger difference, of about 24 nm, that we anticipate can be reduced by changing ink/solvent composition for this compound. We also note that molecular design principles can be applied to fine-tune HOMO–LUMO levels of red absorbing materials to achieve closer match to the long wavelength absorbing cones in the retina.

2.4. Photo-response in the electrolyte to pulsed excitation

Both the sign of charge carriers collected at the ITO electrode and the type of transduction mechanisms, capacitive or faradaic, can be inferred from the pulsed excitation response of devices. Thin film samples on glass ITO/ZnO substrates were mounted inside an electrolyte filled cell (Fig. 4a) and excited with 1 to 50 ms long pulses from three laser diodes emitting at 405 nm, 515 nm and 625 nm wavelength with duty cycles ranging from 50 ms to 999 ms. Time-resolved photovoltage signals were recorded using a pre-amplifier and an oscilloscope. The signals were consistently recorded with negative polarity of the initial spike in samples with the ZnO interlayer on ITO, indicating collection of electrons at the ITO electrode. Capacitive charging of the electrolyte/sample interface can be inferred from the shape of the signal shown in Fig. 6, where the initial spike is coinciding with the beginning of the light pulse, and falling within 5–10 ms time scale, followed by the opposite polarity spike at the end of light pulse. A similar type of response was obtained from all other four molecules' films deposited on ITO/ZnO substrates, consistently showing negative charge carrier collection at ITO and mostly capacitive charging of interfaces.
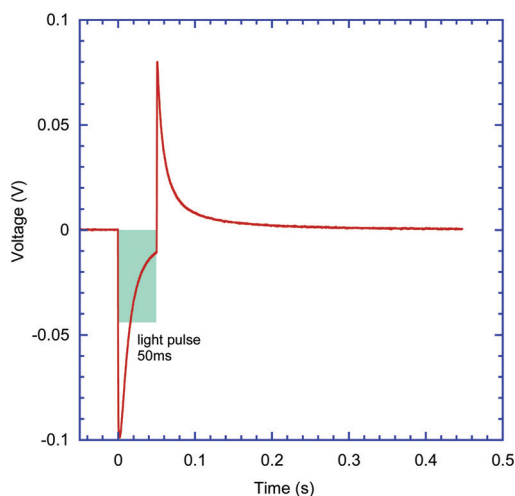

Fig. 6 Transient photo-induced current response of the thin film, GC, **N(Ph-2T-DCV-Hex)₃** sample on glass/ITO/ZnO substrates interfaced with the PBS electrolyte obtained with pulsed excitation from a 515 nm laser diode. Laser pulse width 50 ms, duty cycle 900 ms. The shaded box illustrates the laser pulse width.

An example of typical transient capacitive-response photocurrent for R, **N(Ph-T-CNA-EtHex)₃**, also on the ITO/ZnO substrate, is shown in Fig. S20 (ESI†).

2.5. Charge separation in electrolyte-interfaced devices and the role of substrate work function

Following typical photophysics in organic semiconductors, the absorption of photons with energies higher than the HOMO–LUMO bandgap leads to the creation of excitons, and a heterojunction interface is then required to split the excitons. Considering that devices produced in this work are based on a single organic layer, the interfaces that can contribute to exciton splitting are either organic/substrate or organic/electrolyte. Although the latter might hypothetically have a built-in potential at the electrolyte interface, a significantly stronger effect on photo-induced current and voltage was observed due to work function changes at the substrate-ITO electrode *via* the introduction of interlayers on the ITO surface. Depending on energy level alignment at the small molecule/ITO interface, preferential electron or hole transfer to the ITO, following the photo-excitation process, can be encouraged, especially if charge blocking interlayers such as ZnO are used. The sign of the charge carrier collected at the ITO contact can be inferred from the signal polarity of pulsed excitation tests (Section 2.4). We have observed that with all excitation pulse durations from microseconds to up to 50 ms in our experiments with samples prepared on ITO/ZnO substrates, negative photo-voltage signals persisted, pointing to electron accumulation at the ITO. This result is consistent with previous charge separation studies for short pulse excitation, less than 1 s, at the P3HT/water interface.[46] Bare ITO substrates demonstrated positive polarity signals with strongly pronounced faradaic behaviour, as shown in Fig. S21 (ESI†).

Charge collection at ITO was further supported by varying the effective workfunction of the ITO interface and monitoring the changes in the photocurrent signal. The ITO surface was modified by applying thin layers of PEDOT:PSS with high workfunction and ZnO with low workfunction (Fig. 7). We note that the ZnO interlayer can also work as a hole blocker due to the low-lying valence band edge of ZnO.

The substrate workfunction had a profound effect on the device performance, and this was consistently observed for all four molecules. Photocurrent maxima for **N(Ph-T-CNA-EtHex)₃**, shown here as an example, varied by more than 200 times, with ITO/PEDOT:PSS giving a lower current of only 3 nA, the bare ITO contact resulting in 25 nA current and the ITO/ZnO contact giving the highest current of 670 nA, as shown in Fig. 7a and Table 3. This effect of low-workfunction electrode ITO/ZnO providing the highest photocurrent, and also photovoltage, was found in all devices produced with the four molecules. Considering that the LUMO level of **N(Ph-T-CNA-EtHex)₃** is at −3.35 eV, (Table 1), the ITO/ZnO interface with a workfunction of ∼4 eV[48] provides an optimal heterojunction to split excitons. According to Bassler,[49] 0.3–0.5 eV energy difference between energy levels is needed to dissociate singlet excitons.

5864 | *J. Mater. Chem. C*, 2021, **9**, 5858–5867

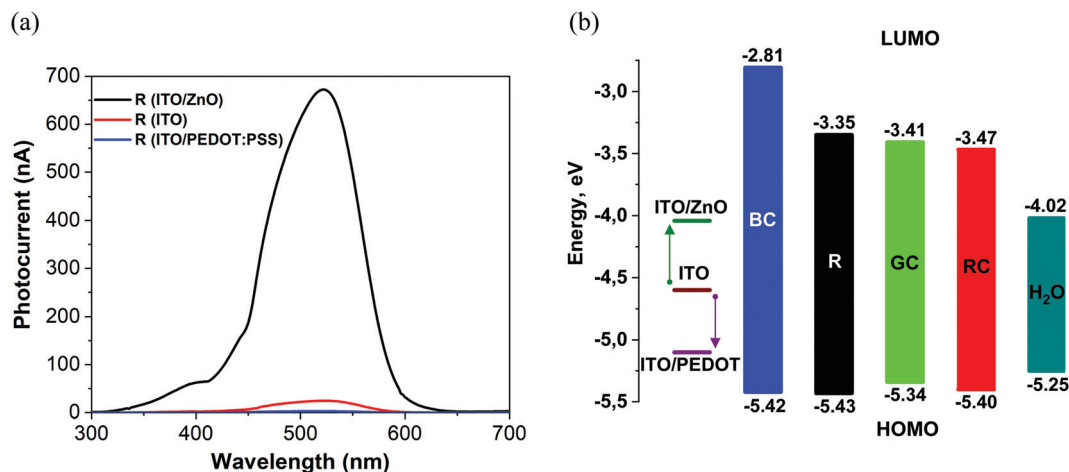This journal is © The Royal Society of Chemistry 2021

(a)

(b)

Fig. 7 (a) Photocurrent spectra of films **N(Ph-T-CNA-EtHex)₃** (R) on glass/ITO/ZnO (black curve), glass/ITO (red curve) and glass/ITO/PEDOT:PSS (blue curve). (b) Flat-band energy band diagram showing the substrate workfunction and HOMO/LUMO levels of **TPA-T-C(O)H** (BC); **N(Ph-T-CNA-EtHex)₃** (R); **N(Ph-2T-DCV-Hex)₃** (RC); **TPA-BTZ-Rh-Et** (RC) and the water splitting potential level E (H+/H₂)[47] (H₂O) at pH 7.

Table 3 The effect of substrate workfunction: photocurrent maxima for **N(Ph-T-CNA-EtHex)₃** films coated on substrates with the following interfaces: ITO, ITO/PEDOT:PSS and ITO/ZnO

Electrode	Estimated workfunction (eV)	Photocurrent (nA)
ITO/ZnO	4.04[48]	670
ITO	4.6[48]	25
ITO/PEDOT:PSS	5.0–5.2[50]	3

The workfunction of bare ITO (4.6 eV)[48] lies close to the middle of the bandgap for R, GC, and RC materials. One can expect that the ITO interface can collect either holes or electrons, depending on the exact energy level alignment. However, the ITO/PEDOT:PSS (5.0–5.2 eV)[50] interface is more favourable for the collection of holes on the ITO side of the junction (Fig. 7b). We note that only very weak positive photocurrent signals have been recorded with ITO/PEDOT:PSS R material devices, with hole collection on the ITO electrode.

To get more insight into charge collection, experimental measurements of hole and electron mobility of all the four materials used were made (see Section 11 in the ESI†). Typical values were between 10^{-4} and 10^{-7} cm² V⁻¹ s⁻¹, with hole mobility being higher than electron mobility for R, GC, and RC materials, and electron mobility being higher than hole mobility for only the BC material (Table S4 in the ESI†). It is quite likely that differences in charge mobility can influence the photo-induced signal magnitude, considering that collection of holes at ITO would have resulted in less efficient electron transport through the films in R, GC, and RC materials. Inversely, collection of electrons at ITO would result in more efficient hole transport through the films in R, GC, and RC materials.

3. Conclusions

We have demonstrated that organic donor–acceptor small molecules with absorption characteristics close to photoresponse bands of human cones and rod cells have excellent potential as functional materials for full colour artificial retina devices. For the future of such devices it is essential that the thin film samples prepared from these semiconducting molecules show photocurrent spectra in the blue, green and red spectral range close to that of human photoactive cells in the retina, when the semiconductor interface is in intimate contact with the bio-compatible electrolyte environment. A key to the potential of full colour vision restoration is the demonstration of photo-induced spectral responses similar to that of rods and cones, obtained at a relatively low light excitation level not exceeding 200 microwatts. Further demonstration of pixelated semiconductor arrays with inkjet printed pixel sizes down to 25 microns shows the feasibility of fabricating artificial retina devices with colour-sensitive, small diameter elements, thus opening opportunities for tailored deposition of multicolour pixel patterns simulating that of real patients' retinas.

Conflicts of interest

There are no conflicts of interest to declare.
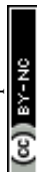
Acknowledgements

References

1 T. R. Fricke, N. Tahhan, S. Resnikoff, E. Papas, A. Burnett, S. M. Ho, T. Naduvilath and K. S. Naidoo, *Ophthalmology*, 2018, **125**, 1492–1499.

2 R. R. A. Bourne, S. R. Flaxman, T. Braithwaite, M. V. Cicinelli, A. Das, J. B. Jonas, J. Keeffe, J. Kempen, J. Leasher, H. Limburg, K. Naidoo, K. Pesudovs, S. Resnikoff, A. Silvester, G. A. Stevens, N. Tahhan, T. Wong and H. R. Taylor, *et al.*, Behalf of the Vision Loss Expert Group, *Lancet Global Health*, 2017, **5**, e888–e897.

3 G. S. Hageman, K. Gaehrs, L. V. Johnson and D. Anderson, Age-Related Macular Degeneration (AMD), *https://webvision.med.utah.edu/book/part-xii-cell-biology-of-retinal-degenerations/age-related-macular-degeneration-amd/*, 2020.

4 NIH, *Retinitis Pigmentosa*, National Eye Institute, 2020, https://www.nei.nih.gov/learn-about-eye-health/eye-conditions-and-diseases/retinitis-pigmentosa.

5 H. Kolb, Simple anatomy of the retina, 2020, https://webvision.med.utah.edu/book/part-i-foundations/simple-anatomy-of-the-retina/.

6 N. Martino, D. Ghezzi, F. Benfenati, G. Lanzani and M. R. Antognazza, *J. Mater. Chem. B*, 2013, **1**, 3768.

7 P. A. Shaposhnik, S. A. Zapunidi, M. V. Shestakov, E. V. Agina and S. A. Ponomarenko, *Russ. Chem. Rev.*, 2020, 89, DOI: 10.1070/RCR4973.

8 T. Someya, Z. Bao and G. G. Malliaras, *Nature*, 2016, **540**, 379–385.

9 S. Löffler, B. Libberton and A. Richter-Dahlfors, *Electronics*, 2015, **4**, 879–908.

10 A. R. Harris and G. G. Wallace, *Adv. Funct. Mater.*, 2018, **28**, 1700587.

11 K. Feron, R. Lim, C. Sherwood, A. Keynes, A. Brichta and P. Dastoor, *Int. J. Mol. Sci.*, 2018, **19**, 2382.

12 K. Liu, Y. Tian and L. Jiang, *Prog. Mater. Sci.*, 2013, **58**, 503–564.

13 J. Rivnay, S. Inal, B. A. Collins, M. Sessolo, E. Stavrinidou, X. Strakosas, C. Tassone, D. M. Delongchamp and G. G. Malliaras, *Nat. Commun.*, 2016, **7**, 11287.

14 D. C. Martin, *MRS Commun.*, 2015, **5**, 131–153.

15 J. F. Maya-Vetencourt, D. Ghezzi, M. R. Antognazza, E. Colombo, M. Mete, P. Feyen, A. Desii, A. Buschiazzo, M. Di Paolo, S. Di Marco, F. Ticconi, L. Emionite, D. Shmal, C. Marini, I. Donelli, G. Freddi, R. Maccarone, S. Bisti, G. Sambuceti, G. Pertile, G. Lanzani and F. Benfenati, *Nat. Mater.*, 2017, **16**, 681–689.

16 M. Ciocca, P. Giannakou, P. Mariani, L. Cinà, A. Di Carlo, M. O. Tas, H. Asari, S. Marcozzi, A. Camaioni, M. Shkunov and T. M. Brown, *Sci. Rep.*, 2020, **10**, 21457.

17 N. S. Sariciftci and S.-S. Sun, *Organic Photovoltaics: Mechanism, Materials, and Devices*, Taylor & Francis, New York, 2005.

18 J. Roncali, P. Leriche and P. Blanchard, *Adv. Mater.*, 2014, **26**, 3821–3838.

19 V. Gautam, D. Rand, Y. Hanein and K. S. Narayan, *Adv. Mater.*, 2014, **26**, 1751–1756.

20 J. F. Maya-Vetencourt, G. Manfredi, M. Mete, E. Colombo, M. Bramini, S. Di Marco, D. Shmal, G. Mantero, M. Dipalo, A. Rocchi, M. L. DiFrancesco, E. D. Papaleo, A. Russo, J. Barsotti, C. Eleftheriou, F. Di Maria, V. Cossu, F. Piazza, L. Emionite, F. Ticconi, C. Marini, G. Sambuceti, G. Pertile, G. Lanzani and F. Benfenati, *Nat. Nanotechnol.*, 2020, **15**, 698–708.

21 M. R. Antognazza, U. Scherf, P. Monti and G. Lanzani, *Appl. Phys. Lett.*, 2007, **90**, 163509.

22 V. Gautam, M. Bag and K. S. Narayan, *J. Am. Chem. Soc.*, 2011, **133**, 17942–17949.

23 E. Castaldi, C. Lunghi and M. C. Morrone, *Neurosci. Biobehav. Rev.*, 2020, **112**, 542–552.

24 A. Mishra and P. Bäuerle, *Angew. Chem., Int. Ed.*, 2012, **51**, 2020–2067.

25 Y. N. Luponosov, J. Min, A. N. Solodukhin, O. V. Kozlov, M. A. Obrezkova, S. M. Peregudova, T. Ameri, S. N. Chvalun, M. S. Pshenichnikov, C. J. Brabec and S. A. Ponomarenko, *Org. Electron.*, 2016, **32**, 157–168.

26 W. Ni, X. Wan, M. Li, Y. Wang and Y. Chen, *Chem. Commun.*, 2015, **51**, 4936–4950.

27 Y. N. Luponosov, A. N. Solodukhin and S. A. Ponomarenko, *Polym. Sci., Ser. C*, 2014, **56**, 104–134.

28 A. N. Solodukhin, Y. N. Luponosov, A. L. Mannanov, P. V. Dmitryakov, S. M. Peregudova, S. N. Chvalun, D. Y. Parashchuk and S. A. Ponomarenko, *Mendeleev Commun.*, 2019, **29**, 385–387.

29 H. T. Bui, D. K. Mai, B. Kim, K.-H. Choi, B. J. Park, H.-J. Kim and S. Cho, *J. Phys. Chem. B*, 2019, **123**, 5601–5607.

30 R. Chennoufi, H. Bougherara, N. Gagey-Eilstein, B. Dumat, E. Henry, F. Subra, S. Bury-Moné, F. Mahuteau-Betzer, P. Tauc, M.-P. Teulade-Fichou and E. Deprez, *Sci. Rep.*, 2016, **6**, 21458.

31 P.-L. Zhang, Z.-K. Wang, Q.-Y. Chen, X. Du and J. Gao, *Bioorg. Med. Chem. Lett.*, 2019, **29**, 1943–1947.

32 Y. Xu, W. Yang, D. Yao, K. Bian, W. Zeng, K. Liu, D. Wang and B. Zhang, *Chem. Sci.*, 2020, **11**, 419–428.

33 A. L. Mannanov, P. S. Savchenko, Y. N. Luponosov, A. N. Solodukhin, S. A. Ponomarenko and D. Y. Paraschuk, *Org. Electron.*, 2020, **78**, 105588.

34 C. Sekirnjak, P. Hottowy, A. Sher, W. Dabrowski, A. M. Litke and E. J. Chichilnisky, *J. Neurophysiol.*, 2006, **95**, 3311–3327.

35 D. Ghezzi, *Front. Neurosci.*, 2015, **9**, 290.

36 J. C. Martins and L. A. Sousa, *Bioelectronic Vision*, World Scientific, 2009, vol. 3.

5866 | *J. Mater. Chem. C*, 2021, **9**, 5858–5867

This journal is © The Royal Society of Chemistry 2021

37 E. Margalit, M. Maia, J. D. Weiland, R. J. Greenberg, G. Y. Fujii, G. Torres, D. V. Piyathaisere, T. M. O'Hearn, W. Liu, G. Lazzi, G. Dagnelie, D. A. Scribner, E. de Juan and M. S. Humayun, *Surv. Ophthalmol.*, 2002, **47**, 335–356.

38 H. J. A. Dartnall, J. K. Bowmaker and J. D. Mollon, *Proc. R. Soc. London, Ser. B*, 1983, **220**, 115–130.

39 File:Cone-response-en.png - Wikimedia Commons, https://commons.wikimedia.org/wiki/File:Cone-response-en.png, 2020.

40 J. K. Bowmaker and H. Dartnall, *J. Physiol.*, 1980, **298**, 501–511.

41 A. Leliège, J. Grolleau, M. Allain, P. Blanchard, D. Demeter, T. Rousseau and J. Roncali, *Chem. – Eur. J.*, 2013, **19**, 9948–9960.

42 E. Ripaud, T. Rousseau, P. Leriche and J. Roncali, *Adv. Energy Mater.*, 2011, **1**, 540–545.

43 O. V. Kozlov, Y. N. Luponosov, S. A. Ponomarenko, N. Kausch-Busies, D. Y. Paraschuk, Y. Olivier, D. Beljonne, J. Cornil and M. S. Pshenichnikov, *Adv. Energy Mater.*, 2015, **5**, 1401657.

44 D. O. Balakirev, Y. N. Luponosov, A. L. Mannanov, P. S. Savchenko, Y. Minenkov, D. Y. Paraschuk and S. A. Ponomarenko, *Dyes Pigm.*, 2020, **181**, 108523.

45 K. Murata and K. Masuda, *Convert. e-Print*, 2011, **1**, 108–111.

46 E. Mosconi, P. Salvatori, M. I. Saba, A. Mattoni, S. Bellani, F. Bruni, B. Santiago Gonzalez, M. R. Antognazza, S. Brovelli, G. Lanzani, H. Li, J.-L. Brédas and F. D. Angelis, *ACS Energy Lett.*, 2016, **1**, 454–463.

47 P. Peljo and H. H. Girault, *Energy Environ. Sci.*, 2018, **11**, 2306–2309.

48 A. Sharma, M. Untch, J. S. Quinton, R. Berger, G. Andersson and D. A. Lewis, *Appl. Surf. Sci.*, 2016, **363**, 516–521.

49 H. Bässler, V. I. Arkhipov, E. V. Emelianova, A. Gerhard, A. Hayer, C. Im and J. Rissler, *Synth. Met.*, 2003, **135–136**, 377–382.

50 PEDOT:PSS | PH 1000, Al 4083, HTL Solar & HTL Solar 3 | Ossila, https://www.ossila.com/products/pedot-pss?variant=30366225236064 (accessed 9 November 2020).

This journal is © The Royal Society of Chemistry 2021

J. Mater. Chem. C, 2021, **9**, 5858–5867 | **5867**